Allying topology and shape optimization through machine learning algorithms

D. Muñoz, E. Nadal, J. Albelda, Francisco Chinesta, J.J. Ródenas

Allying topology and shape optimization through machine learning algorithms

D. Muñoz [a,*], E. Nadal [a], J. Albelda [a], F. Chinesta [b], J.J. Ródenas [a]

[a] Institute of Mechanical and Biomechanical Engineering (I2MB), Universitat Politècnica de València, Building 5E, Camino de Vera s/n, 46022, Valencia, Spain
[b] ESI Chair, PIMM, Arts et Métiers Institute of Technology, 151 Boulevard de l'Hopital, F-75013, Paris, France

ARTICLE INFO

Keywords:
Topology optimization
Mesh refinement
H-adaptivity
cgFEM
Shape optimization
Hybrid optimization
Machine learning
Dimensionality reduction
Locally linear embedding

ABSTRACT

Structural optimization is part of the mechanical engineering field and, in most cases, tries to minimize the overall weight of a given design domain, subjected to functionality constraints given in terms of stresses or displacements. The most relevant techniques are topology and shape optimization. Topology optimization provides the optimal material distribution layout into a given, static, design domain. On the other hand, shape optimization provides the optimal combination of the parameters that define the required parametrization of the domain's boundary. Both techniques have strengths and weaknesses, thus a hybrid optimization approach that combines the former techniques will define a more general structural optimization framework that will take advantage of their synergistic combination. The difficulty arises when communicating both techniques for which, in this paper, we propose a machine learning-based methodology.

1. Introduction

Optimization is the mathematical discipline that tries to find the best element of a given set. The search is driven by the performance of each element, measured through a predefined loss function. Optimization techniques are extensively used in fields such as science, engineering or economics. We will focus on the engineering field, specially on structural optimization. Structural optimization is a crucial tool in the design process of mechanical components, since it is able to generate the optimal design domain according to a set of applied loads. The optimal design must minimize or maximize an objective function while satisfying a set of constraints. The most common pairs of objective function and constraints found in the structural optimization field are: the minimization of the mass/volume while satisfying a yielding stress constraint and the maximization of the stiffness while satisfying a volume fraction constraint. There exist different approaches to solve the structural optimization problems. Among them, we will focus on the most common ones, namely, topology and shape optimization techniques.

Topology optimization algorithms allow to modify the topology of the material in the design space at the expense of a large amount of design variables, such as the relative density of each element with the SIMP method [1–3], the distance of each node to the implicit boundary with the Level-Set approaches [4–6] or the Phase Field for topology optimization [7–9]. The current work is based on the SIMP method that provides an optimal material distribution layout over the design domain defined by a blurred boundary which is not directly suitable for manufacturing. A review of the SIMP method can be found in Appendix A.1. On the other hand, shape optimization techniques, use a CAD representation of the boundary of the geometry to compute the objective function and constraints. This CAD representation may be defined using many types of geometrical entities (splines, NURBS, etc.). In our case, the boundary will be represented using the STL format, i.e., a triangular tessellation of the geometric boundary. Thus, the optimal geometry provided is directly suitable for manufacturing. In this work, we consider the parameterized shape optimization algorithm which needs a user-defined parameterized boundary of fixed topology that does not allow to explore new topologies. The main benefit of using shape optimization techniques is the accuracy and smoothness of the boundary definition. This benefit is even greater if we take into account that the number of design variables necessary to parameterize the boundary of the geometry is usually low, this allowing the exploration of the design space with a huge variety of optimization algorithms. A description of the shape optimization problem considering geometrical

parameters can be found in Appendix A.2.

Given the characteristics of these two types of optimization techniques, it would be desirable to develop a hybrid approach that harness the strengths and discards the weaknesses of the topology and shape optimization techniques when used separately.

This hybrid algorithm could be defined by the following steps:

1. Topology optimization. This step should provide a preform with topological characteristics defined in terms of an optimal material distribution layout, consider the design domain defined by the analyst.
2. Interface. This step should communicate both topology and shape optimization algorithms. This interface should generate the parametric geometrical model (defined by design variables) required by the shape optimization algorithm from the results of the topology optimization process.
3. Shape optimization. The shape optimization algorithm should then use this model and will find the optimal combination of its parameters that minimize a given objective function while satisfying the prescribed constraints. The final results of this step should be a CAD-like representation of the optimal geometry directly suitable for manufacturing.

The main issue that we face when implementing such a hybrid algorithm is the development of step 2, the interface step, that allies both topology and shape optimization algorithms. Below are, to the authors' knowledge, the main contribution to this topic that can be found in the bibliography. Reference [10] manually parametrized the result of the topology optimization solution, and used it in the parametrized shape optimization algorithm. In the approach described in Refs. [11,12], the authors parametrize the optimal material distribution of a 2D design domain by means of curve fitting algorithms. The parameters that define those curves are then modified by the shape optimization algorithm to find the optimal geometry. Also, we would like to highlight the work in Ref. [13] where the use of Artificial Neural Networks allow to find the set of simple entities that reproduce the material distribution provided by the topology optimization algorithm. Additionally, alternative approaches are found in the literature. For instance, in Ref. [14] the authors use an edge detection technique to identify the structural elements provided by the topology optimization algorithm. In Ref. [15] the authors use a edge detection technique, the Canny algorithm, and manually create a B-spline representation of the model. In Ref. [16] the authors manually create the mesh for the shape optimization algorithm by means of the material distribution layout indicated by the topology optimization algorithm. Also, in Ref. [17] the authors simultaneously evaluate both optimization algorithms; in this case the shape is modified considering the variation of the nodal coordinates of the mesh by means of weights, acting as design variables, and predefined perturbation vectors. In Refs. [18,19], the authors create a two-stage algorithm where the overall geometric definition is achieve in the topology optimization step. Then the result is represented with Deformable Simplicial Complex entities whose vertices' positions can be modified by the shape optimization algorithm. Also [20], presented a new level-set algorithm that allows to reduce the dimension of the functional by means of the Radial Basis Functions. Finally, we highlight the interesting work developed in Ref. [21] where the authors propose to first use a shape optimization algorithm to define the design domain and then to use a topology optimization algorithm to find the optimal material distribution.

In our work, we propose the use of a Machine Learning (ML) technique to infer the geometrical characterization defined by a set of parameters. Specifically, we use a Dimensionality Reduction (DR) algorithm, a subfield of the ML techniques. These algorithms will automatically create a parametric model, defined as a combination of geometrical modes that explicitly characterizes the implicit boundary given by the material distribution provided by the topology optimization algorithm. The extracted geometrical features may take the form of simple geometrical entities, such as radius or thickness but, in general, the extracted geometrical features will be more complex. In any case, the ML tool will be able to identify the geometrical modes, providing a parametric geometrical representation. We will then be able to use this parametric characterization to generate new geometries by modifying the value of the parameters, either manually or guided by an external algorithm. In our case, we will introduce these parameters as the design variables used by a shape optimization algorithm.

The paper is organized as follows. The implementation of the hybrid optimization algorithm relies on a set of technologies or methods, that are presented in *Section* 2. Following, in *Section* 3, we will describe the benchmark analytic problem used to check the functionalities developed. Then, in *Section* 4 we will describe the strategy considered to achieve an hybrid optimization framework and how the previously described technologies interact with each other. Later, in *Section* 5 we will show the behaviour of the proposed methodology by means of numerical analyses considering the benchmark problem together with the numerical analyses on the well-known MBB beam problem and a hook problem. Finally, in *Section* 6, we will conclude the paper with some final remarks. An *Appendix* is also included, for the sake of completeness, to properly describe some methods and technologies discussed in this work.

2. Methodologies

As proposed in *Section* 1, our goal is to ally topology and shape optimization techniques in order to develop a hybrid optimization framework. To accomplish this objective, we will make use of different methodologies and technologies.

On one hand, we will harness the capabilities of Machine Learning (ML) techniques to infer information from datasets.

The topology optimization technique produces intermediate solutions during the iterative process. After the initial steps of the process, characterized by substantial modification of the solution, i.e., once the final convergence to the solution has started, the intermediate solutions will only undergo minor modifications around the final solution. Then, we propose to consider these solutions obtained from the iterative process as snapshots that will be used by a ML algorithm to infer the characteristics of the geometry provided by the TO technique. We will use the parameters associated to the geometrical modes to generate new geometries, not existing in the original dataset. The generation of the new geometries may be guided through a shape optimization technique, accordingly, obtaining an optimal geometry suitable for manufacturing. In order to achieve this objective, we rely on the Dimensionality Reduction (DR) algorithms, a sub-field of ML. There exist a huge variety of techniques in the DR field, such as the Principal Component Analysis (PCA) [22], which finds the directions of maximum variation in the original dataset. The former algorithm is a linear technique, mainly used some time ago, but currently non-linear techniques have been developed to obtain the inherent structure of the dataset. These techniques can preserve the non-linear behaviour of the initial dataset, such as the Locally Linear Embedding (LLE) [23] (see Appendix A.3). In this work we use the LLE to compute the manifold space. As the geometrical modes indicate the directions of the geometry evolution towards the minimization of the fitness function, we will use the parameters associated to the geometrical modes to generate new geometries, not existing in the original dataset.

On the other hand, the main concerns about structural optimization are its efficiency and accuracy. Therefore, we use the *cgFEM* framework to compute the FE calculations. In short, *cgFEM* [24,25] is a Fictitious Domain Method (FDM) [26–28], thus the domain discretization is considered over an easy-to-mesh fictitious domain that embeds the physical domain. In *cgFEM*, this embedding domain is a cube and the mesh is obtained by using a set of Cartesian grids. The inherent hierarchical structure of mesh allows to easily share information between elements or meshes. Thanks to the use of the Cartesian grids, all elements

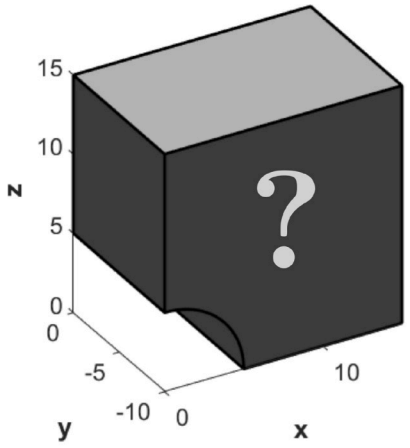

(a) Model of the 3D domain used for the optimization problem. Symmetry boundary conditions on planes $x = 0$, $z = 0$, and also on $y = 0$ and $y = -10$ to represent the plane strain condition.

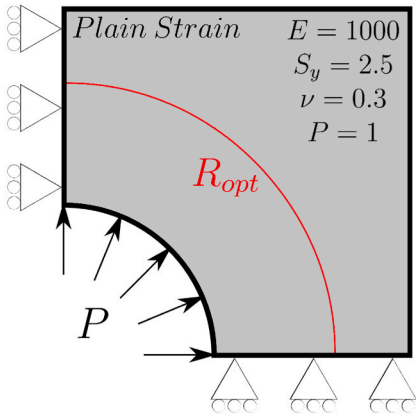

(b) 2D view of the optimization problem, including optimal analytical external boundary (in red) with value $R_{opt} = 9.0468$.

Fig. 1. Reference problem.

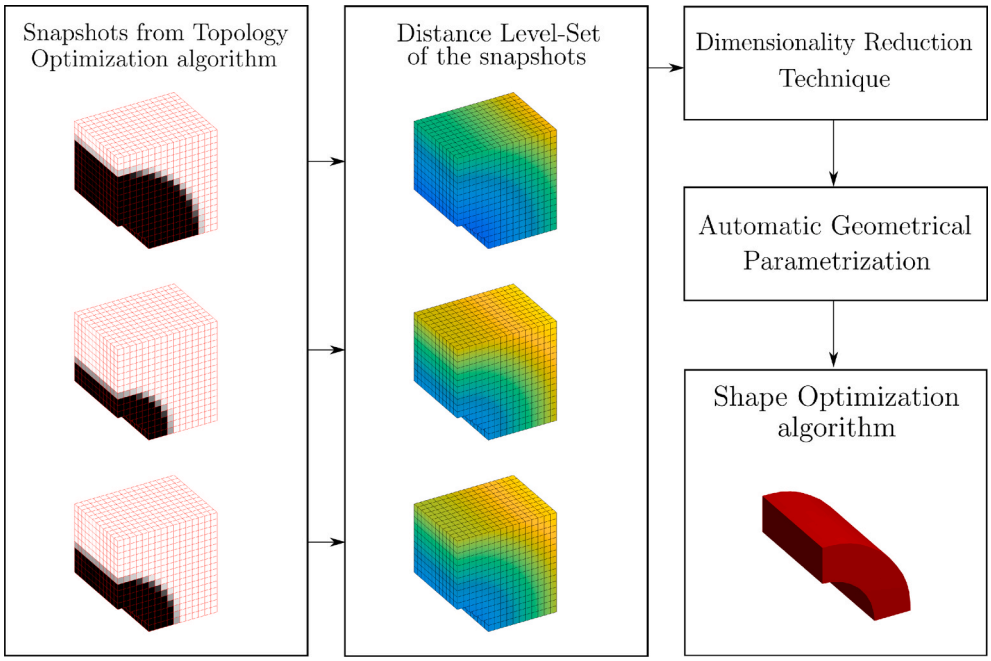

Fig. 2. Hybrid optimization workflow.

in the mesh are regular hexahedrons. This particular feature decreases drastically the computational effort devoted to integration, as the information of one element may be shared with the rest. Appendix A.4 conscientiously review the *cgFEM*.

3. Reference benchmark problem

The reference problem used to describe the proposed methodologies is defined in Fig. 1 where we use a coherent system of units. This problem corresponds to a constant hollowed cross sectional area beam, with 2 perpendicular planes of symmetry ($x = 0$ and $z = 0$), under plain strain conditions, subjected to a pressure P on the internal cylindrical surface.

The objective of the optimization problem is to minimize the amount of material while the maximum von Mises stress value ($\max(\sigma_{vm})$) is equal to the yield limit (S_y). It is known that the optimal shape will also correspond to a circular external shape, i.e., the optimal shape will take the form of a thick-walled cylinder. The following equations are the analytical solutions for displacements (1) and stresses (2) of thick-walled cylinders subjected to internal pressure [29]:

$$\boldsymbol{u} = \begin{Bmatrix} u_R\cos(\theta) \\ 0 \\ u_R\sin(\theta) \end{Bmatrix} \quad u_R = \frac{P(1+\nu)}{E(\kappa^2-1)}\left[\left(1-2\nu\right)r + \frac{r_{ext}^2}{r}\right] \tag{1}$$

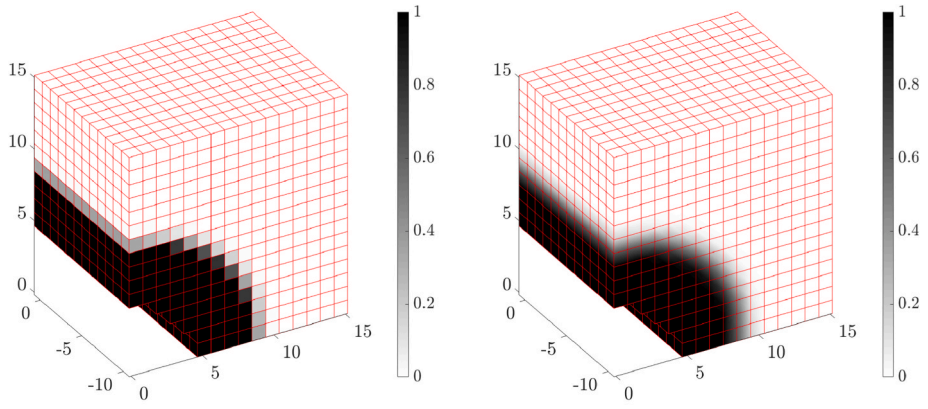

(a) Topology optimization result (b) Nodal projection

Fig. 3. Reference problem. Optimal topology optimization material distribution (a) with its nodal projection equivalent (b).

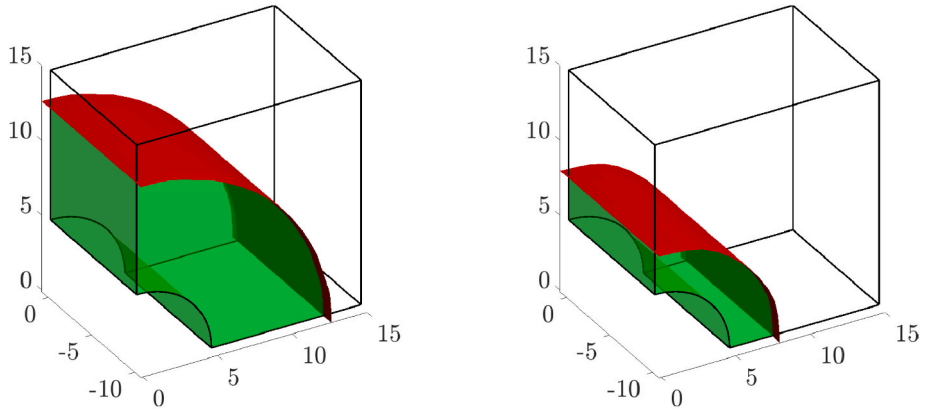

(a) (b)

Fig. 4. MC polygonal meshes representing the external cylindrical shape of the solution obtained from the material distribution considering an isovalue $\rho_c = 0.5$, for v_f equal to 0.5 (a) and 0.15 (b).

$$\boldsymbol{\sigma} = \begin{Bmatrix} \sigma_R \cos(\theta)^2 + \sigma_H \sin(\theta)^2 \\ \nu(\sigma_x + \sigma_z) \\ \sigma_R \sin(\theta)^2 + \sigma_H \cos(\theta)^2 \\ 0 \\ 0 \\ (\sigma_R - \sigma_H)\sin(\theta)\cos(\theta) \end{Bmatrix} \quad \begin{aligned} \sigma_R &= \frac{P}{\kappa^2 - 1}\left[1 - \left(\frac{r_{ext}}{r}\right)^2\right] \\ \sigma_H &= \frac{P}{\kappa^2 - 1}\left[1 + \left(\frac{r_{ext}}{r}\right)^2\right] \end{aligned} \tag{2}$$

where $r = \sqrt{x^2 + z^2}$ is the radius of a point of coordinates (x, y, z) in the domain, r_{ext} and r_{int} are the external and internal radii, $\kappa = r_{ext}/r_{int}$, $\theta = \arctan(z, x)$, E is the Young Modulus and ν is the Poisson's ratio.

The maximum von Mises stress in the cylinder can be evaluated, considering the exact solution in stresses, as a function of the external radius. Therefore, it is possible to find the value of the minimum external radius that satisfies $\max(\sigma_{vm}) \leq S_y$. For the data shown in Fig. 1, this radius is $R_{opt} = 9.0468$, represented in Fig. 1, that leads to an optimum volume $V_{opt} = 446.4545$.

4. Hybrid optimization

In this section we will describe the details about the strategy that we propose to ally topology and shape optimization techniques and to create a general structural optimization framework. We will describe the procedure developed to automatically extract the geometrical parameters and how we use them. In Fig. 2, we show the main steps in the proposed strategy.

To summarize, as represented in Fig. 2, we postprocessed the material distribution layout provided by the TO algorithm to create a distance level-set. This level-set has the information of the distance between each node to the implicit boundary. Then, the level-set is used to extract the geometrical modes by using a DR tool. This process is based on the procedure presented in Ref. [30] where, using a set of **X** segmented images of livers, a DR technique, trained to infer the shape of livers provided a parametrized model to represent livers based on just two parameters. Finally, using the reduced parametric geometrical model, the procedure is able to reconstruct a CAD geometry and, thus, to use a standard parametric shape optimization tool to obtain the final geometry, both topologically and structurally optimized.

4.1. Dimensionality reduction. Parametrization

Topology optimization algorithms provide an optimal material distribution layout of the design domain, i.e. the material/void status of each element considered in the discretization. In our case, based on the SIMP method, the elements also may have intermediate relative densities, representing fictitious material properties. We want to infer the geometry of the solution provided by the TO algorithm, described by a large number of parameters (one relative density per element) and to describe it using a reduced number of parameters. Hence, we will use a

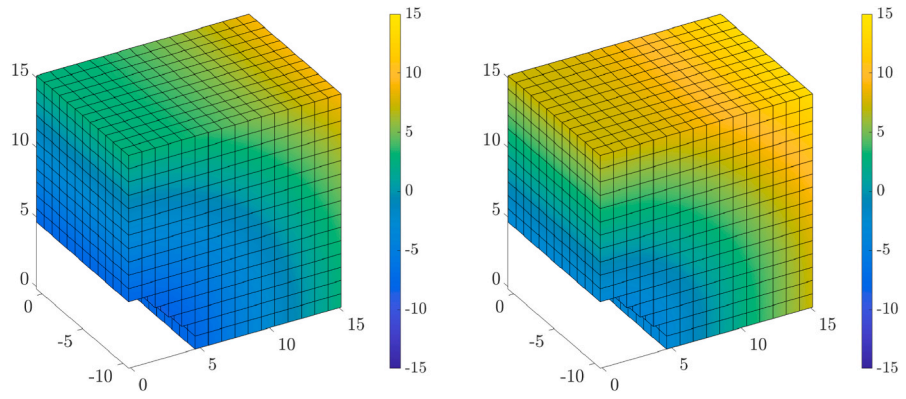

(a) Distance function obtained from the boundary shown in Figure 4a

(b) Distance function obtained from the boundary shown in Figure 4b

Fig. 5. Distance function to the boundary, represented as a value equal to 0, obtained from Fig. 4.

ML algorithm to reduce the dimensionality of the solution. The training process of a ML algorithm requires the use of a sufficiently large amount of snapshots, each of them representing the geometry to be inferred. As most optimization techniques, TO is an iterative method, which means that the material distribution information of each iteration will be available. Once the TO process has started to converge, there will only be minor changes in the material distribution, that will be very similar to that of the final solution and, therefore, with the same topology. Hence, these intermediate material distributions of the iterative process will be suitable for the ML tool, that will be able to describe the geometry using a reduced number of parameters, each of them associated to a geometrical mode. The choice of snapshots is arbitrary, as far as all of them maintain the same topology. The strategy followed in this work is to select the last iterations from the topology optimization process, thus mainly ensuring the topology invariance while detecting the evolution of the geometry in these last steps. As each snapshot can have different size, we propose to project the information of each snapshot to a common uniform mesh of elements having the size of the smallest element used in the definition of the snapshots. Thanks to the Cartesian grid and the hierarchical data structure of *cgFEM*, this projection process is costless and straightforward.

In Fig. 3a, we show the optimal material distribution layout provided by the TO algorithm for the Benchmark problem. Although, in this example there will be no change in the topology, but it will help us to illustrate the procedure. The element-wise solution directly provided by the TO algorithm, will be first smoothed using nodal averaging procedure, whose result is show in Fig. 3b, to obtain a nodal representation.

As shown in Fig. 3b, the field represented over the design domain is quasi-boolean, so the information it provides is very limited. To solve this problem, this information must be postprocessed in order to obtain a much richer information given by the distance of each node to the implicit boundary. As the boundary in the regions with intermediate values of ρ is not explicitly defined, we have to generate an explicit geometrical definition. To do it, we use the Marching Cubes (MC) [31] algorithm that provides a polygonal mesh from the isosurfaces, defined by an isovalue ρ_c, existing in the material distribution with $\rho_c \in [0, 1]$. Fig. 4 represents the polygonal mesh obtained from the MC algorithm for different values of v_f for an isovalue $\rho_c = 0.5$ in both cases. The final volume is represented by the isosurface of selected value of ρ_c in the regions with intermediate values of ρ (red surface in Fig. 4) and by the regions of the CAD surface that define the design space with $\rho = 1$ (green transparent surfaces in Fig. 4).

Once the surface defining the volume has been evaluated, the solutions represented by nodal densities are replaced by the level-set information that represents the distance of each node to the surface. In Fig. 5, we represent the distance level-set obtained from the cases represented in Fig. 4. With this procedure we transformed the quasi-boolean information of the material distribution into a smooth and monotonous level-set.

In the original algorithm of the SIMP method (see Algorithm 1 in Appendix A.1) the volume fraction is set as a constraint and the compliance is minimized. The algorithm will only provide a limited exploration of the design space as a single value of the volume fraction will be considered. Additionally, as no further constraints are taken into account, the outcome of the algorithm is not fully useful for structural applications where, for example, stress constraints are very common. To ensure design richness, we have implemented a simple, not fully robust implementation of a TO algorithm, where a heuristic stress scaling technique, not to be compared with a stress constraint, adapts the volume fraction to target a given maximum stress value, for instance the yield limit [32]. It must be taken into account that this simple strategy, not suitable for problems with stress singularities, is not a procedure to impose stress constraints, which would require a consistent treatment of the stress gradients, including a regularization of the stress field [33,34] and a more advanced optimization algorithm. These more advanced algorithms could also be considered, but they are out of the scope of the paper as we simply need a basic exploration of the design space considering appropriate volume fractions. Hence, we propose the use of Algorithm 2 defined in Appendix A.1. Algorithm 2 consists of two nested loops. The inner loop follows the strategy of the original SIMP method and produces solutions of minimum compliance, subjected to the volume fraction constraints dictated by the outer loop. The main benefit of using this approach within the hybrid optimization framework is that it will automatically increase the richness of the snapshots dataset by extending the exploration of the design space varying the values of the volume fraction that will tend to increase the density of the snapshots around the vicinity of the optimal volume fraction.

We also propose to increase the number of snapshots, by simply repeating the previous strategy. Considering, for each material/void layout different values of ρ_c. The snapshots chosen to train the DR model are arbitrary, but all of them must have the same topology. Once the snapshots have been evaluated as previously described, we will use them as the training dataset for the DR model, specifically for the LLE algorithm, as indicated. LLE algorithm is a DR technique that extracts the embedded manifold structure existing in a high-dimensional space, which in our case is defined by the distance level-set. This embedded manifold or low-dimensional space will be defined by a set of parameters. We will consider that these parameters characterize and describe the geometrical features of our preform. Let $\mathbf{X}_i$ be each of the training high-dimensional points (or snapshots). The LLE hypothesize that any

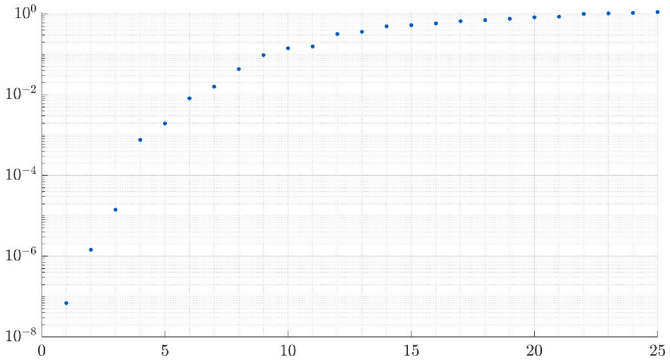

Fig. 6. Reference Problem. First 25 eigenvalues of **M** (see (6)), in the LLE procedure.

point may be obtained as a linear combination of K neighbours with W_{ij}, $j \in [1, K]$. The number of neighbours K is user-defined and the weights are obtained by minimizing the functional represented in equation (3):

$$e(\mathbf{W}) = \sum_i \|\mathbf{X}_i - \sum_j W_{ij}\mathbf{X}_j\|^2, \tag{3}$$

where W_{ij} are subjected to the constraint $\sum_j W_{ij} = 1$. The LLE entrusts that these weights are invariant to space transformations. Hence, the value of the weights is preserved when changing between spaces. Now, the low-dimensional parameters may be obtained by minimizing the functional in (4):

$$\varphi(\mathbf{Y}) = \sum_i \|\mathbf{Y}_i - \sum_j W_{ij}\mathbf{Y}_j\|^2, \tag{4}$$

where $\mathbf{Y}_i$ represent each of the points projected to the embedded space. The former equation may be represented in the form shown in (5):

$$\varphi(\mathbf{Y}) = \mathbf{Y}^T\mathbf{M}\mathbf{Y}, \tag{5}$$

with,

$$\mathbf{M} = (\mathbf{I} - \mathbf{W})^T(\mathbf{I} - \mathbf{W}). \tag{6}$$

The minimization problem could be considered as an eigenvalue problem, where the eigenvectors represent the low-dimensional points **Y**. The dimension of the embedded space may be a user-defined parameter, but it is convenient to study the eigenvalues of **M**. As we minimize (5), the target eigenvectors are related to the smallest eigenvalues, as shown in Fig. 6, we define the dimensionality as $d = 1$ because the first eigenvalue is far from the following. The detailed mathematical procedure to obtain the low-dimensional embedded space is explained in Ref. [35].

Fig. 7 shows the embedded space obtained by this technique applied to the reference problem. The y-axis represents the volume of the final geometry whereas the x-axis represents the extracted low-dimensional parameter. We used $K = 21$ neighbours from a total amount of 101 individuals (snapshots). The colours of the graph in Fig. 7 represents the

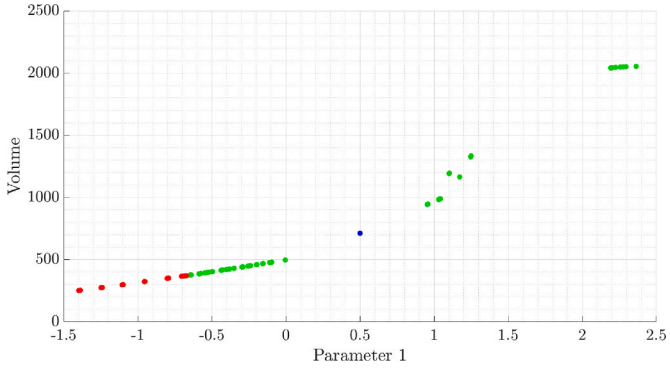

Fig. 7. Reference problem. Embedded space[1] for the reference problem considering $K = 21$ neighbours and $d = 1$ parameters. The y-axis represents the volume of each individual, while the colour represents if the maximum stress value is below (green) or above (red) the yield stress limit. (For interpretation of the references to colour in this figure legend, the reader is referred to the Web version of this article.)

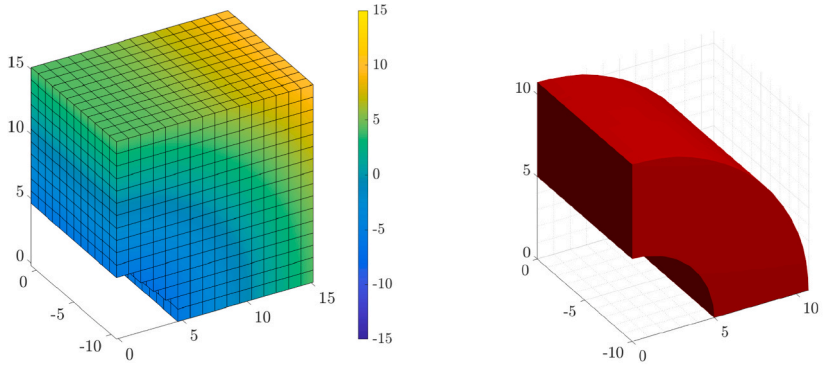

(a) Distance level-set.

(b) Representation of the geometry recovered from the level-set.

Fig. 8. Reference problem. New geometry obtained from the ispace transformation of $\widehat{\mathbf{Y}}_i$ into $\widehat{\mathbf{X}}_i$.

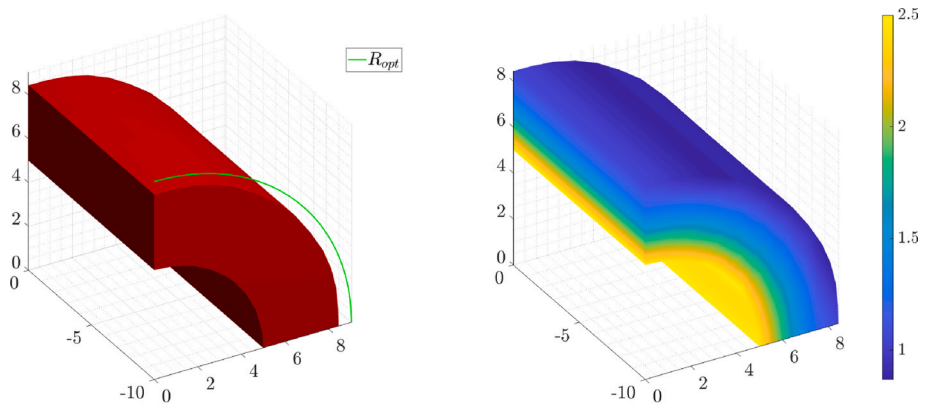

(a) Final geometry (b) Von Mises stress

Fig. 9. Reference problem. Optimal geometry (in red) from the hybrid optimization algorithm with the optimal analytic radius (in green) $R_{opt} = 9.0468$ (a) and the recovered von Mises stress field (b) The results were obtained using meshes of element size $h_{\mathbb{TO}} = h_{\mathbb{SO}} = 0.9563$. (For interpretation of the references to colour in this figure legend, the reader is referred to the Web version of this article.)

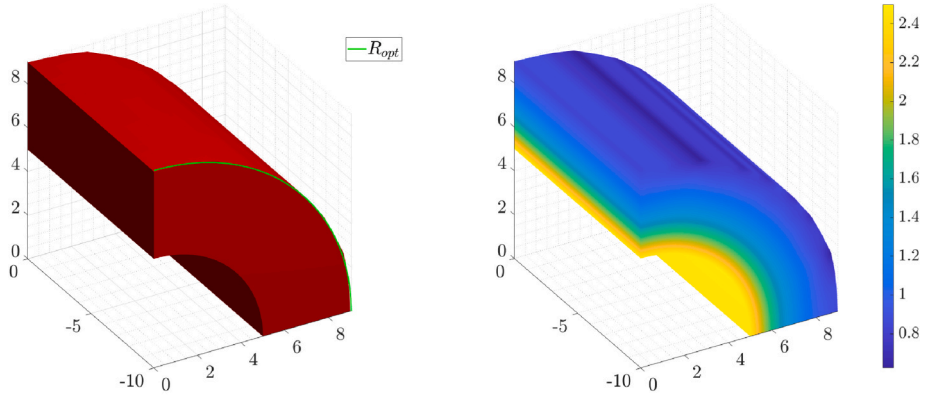

(a) Final geometry. (b) Recovered von Mises stress field.

Fig. 10. Reference problem. Hybrid optimization result of the reference problem with the optimal analytic radius $R_{opt} = 9.0468$ (a) and Von Mises stresses (b). The results were obtained using meshes of element size $h_{\mathbb{TO}} = 0.9563$ and $h_{\mathbb{SO}} = 0.2391$.

Table 1
Reference Problem. Relative time comparison for the different analysis considered. $\mathbb{TO}(v_f(S_y))$ stands for the Topology Optimization process where the v_f scales the von Mises stress to target S_y, $\mathbb{MG}$ represents the Model Generation procedure and $\mathbb{SO}_\sigma(S_y)$ refers to the Shape Optimization process defined by (9a) and (9b). The column Total is the accumulated processing time. The last column represents the relative error ($err(R)$) in the radius with respect to the optimal analytical radius for each analysis obtained as $err(R) = \dfrac{R - R_{opt}}{R_{opt}} \times 100$.

	Relative time				$err(R)$ (%)
	$\mathbb{TO}(v_f(S_y))$	$\mathbb{MG}$	$\mathbb{SO}_\sigma(S_y)$	Total	
$h_{\mathbb{TO}} = 0.9563$; $h_{\mathbb{SO}} = 0.9563$	1	1	1	1	−5.1862
$h_{\mathbb{TO}} = 0.9563$; $h_{\mathbb{SO}} = 0.4781$	1	1.333	2.4943	1.5894	−0.0971
$h_{\mathbb{TO}} = 0.9563$; $h_{\mathbb{SO}} = 0.2391$	1	3.9167	14.3239	6.2539	0.0101
$h_{\mathbb{TO}} = 0.4781$; $h_{\mathbb{SO}} = 0.4781$	4.6415	12.2500	3.7898	4.5121	−0.8554
$h_{\mathbb{TO}} = 0.4781$; $h_{\mathbb{SO}} = 0.2391$	4.6415	14.8333	15.3864	9.0861	−0.0043
$h_{\mathbb{TO}} = 0.2391$; $h_{\mathbb{SO}} = 0.2391$	54.4868	187.3333	13.5739	42.1104	−0.0021

feasibility of the individuals, green points denote structures with maximum stress below the (yield) stress limit while red points have von Mises stresses above the yield limit S_y.

4.2. Generation of new geometries

We have obtained a low-dimensional embedded manifold that defines the geometrical characteristics of the material distribution. Our goal is to use this information to create CAD representations of the geometry. Hence, we define the value of a set of parameters $\widehat{\mathbf{Y}}_i$ in the embedded space $\mathbf{Y}$. This point may be user-defined, however the interesting part of this approach is that it can be automatically defined by an algorithm, e.g. a shape optimization algorithm. We hypothesize that $\widehat{\mathbf{Y}}_i$ is a weighted interpolation between a set of $\widehat{K}$ neighbours. The value of interpolation weights $\widehat{W}_{ij}$ is obtained minimizing the functional,

$$e(\widehat{W}) = \sum_i \|\widehat{\mathbf{Y}}_i - \sum_j \widehat{W}_{ij}\mathbf{Y}_j\|^2 \tag{7}$$

In this case, we assume, as in the LLE technique, that weights $\widehat{W}_{ij}$ are

[1] Notice that the design space is not fully represented as it depends on the exploration performed by the topology optimization algorithm.

Table 2
Reference Problem. Comparison of solutions obtained with each analysis. The green curve corresponds to the optimal analytical radius $R_{opt} = 9.0468$.

$\mathbb{TO}_\sigma(S_y)\backslash\mathbb{SO}_\sigma(S_y)$	$h = 0.9563$	$h = 0.4781$	$h = 0.2391$
$h = 0.9563$	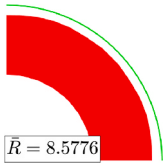 $\bar{R} = 8.5776$	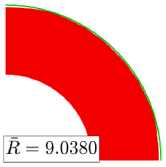 $\bar{R} = 9.0380$	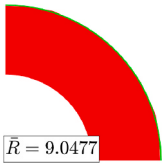 $\bar{R} = 9.0477$
$h = 0.4781$	–	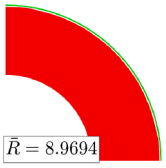 $\bar{R} = 8.9694$	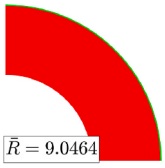 $\bar{R} = 9.0464$
$h = 0.2391$	–	–	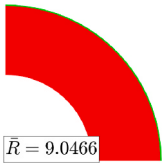 $\bar{R} = 9.0466$

invariant to space transformations. As we have computed the neighbours $\boldsymbol{Y}_j$, we gather the matching high-dimensional points $\boldsymbol{X}_j$. Finally, we apply the following weighted interpolation to compute $\widehat{\boldsymbol{X}}_i$, i.e., a level-set of the new geometry defined in the high-dimensional space:

$$\widehat{\boldsymbol{X}}_i = \sum_j \widehat{W}_{ij} \mathbf{X}_j \tag{8}$$

In order to show how the geometries are generated, we select a point $\widehat{\boldsymbol{Y}}_i = 0.5$ that belongs to the embedded space created by $\mathbf{Y}$. In Fig. 7, we show the individual $\widehat{\boldsymbol{Y}}_i$ (in blue) in its space $\mathbf{Y}$. This procedure provides as a result a new point located in the high-dimensional space $\mathbf{X}$, called $\widehat{\boldsymbol{X}}_i$. The individual $\widehat{\boldsymbol{X}}_i$ has the distance information of each node to the boundary of the geometry, as represented in Fig. 8a. We harness this information to compute the boundaries that define the new geometry, as shown in Fig. 8b.

A clearer understanding of the influence of the geometric modes using this procedure can be obtained through the example shown in *Section* 5.1, where a more complex geometry has been considered.

4.3. Shape optimization

In previous sections, we have presented a procedure to automatically parametrize the material distribution from the topology optimization and to extract the main geometrical features (Section 4.1). We have also shown how this parametrization is used to generate new geometries (Section 4.2). This strategy has interest in itself, as we are able to generate new geometries not existing in the training set of data. As the purpose of this paper is to ally topology and shape optimization techniques, we propose a final step where the modification of the parameter $\widehat{\boldsymbol{Y}}_i$ is guided by the updating scheme of a shape optimization algorithm, the minimization of the volume into the region of feasible design where the maximum von Mises stress value is below the prescribed yield limit.

As we have defined our implicit parametrization of the boundary of the design domain, our shape optimization problem can be expressed with the following equation,

$$(\mathbb{SO}_\sigma(S_y)) = \begin{cases} \min\limits_{\widehat{\boldsymbol{Y}}}: & \text{Volume}(\widehat{\boldsymbol{Y}}) & \text{(9a)} \\ \text{subjected to:} & max(\sigma_{eq}(\widehat{\boldsymbol{Y}})) = S_{cr} & \text{(9b)} \end{cases}$$

where σ_{eq} represents an equivalent stress value and S_{cr} is the limit value of σ_{eq}. For example, the stress value used in this paper is the recovered von Mises stress σ^*_{vm} while the limit value is equal to the yield limit S_y.

Once we have expressed the geometry as a function of a reduced set of design variables, as if we were having a parametrized CAD model, we

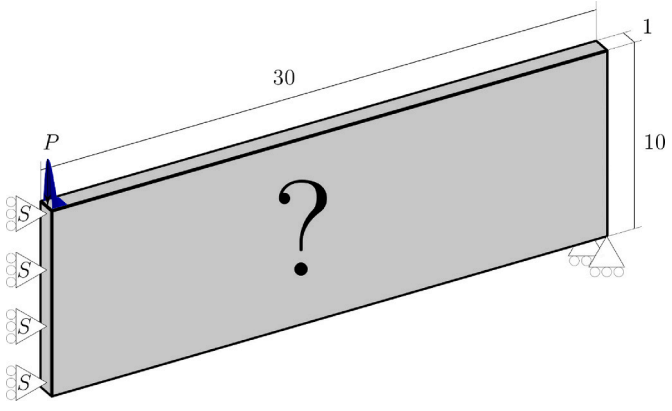

Fig. 11. MBB problem.

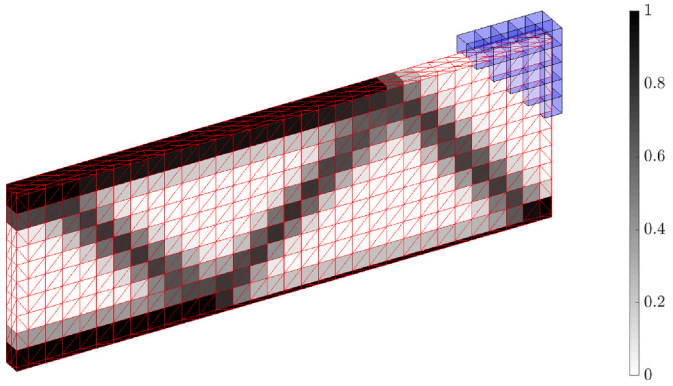

Fig. 12. MBB Problem. Optimal material distribution layout from the topology optimization algorithm, obtained with a uniform mesh of non-conforming hexahedra of size $h_{\mathbb{TO}} = 0.9563$, represented on the conforming tetrahedra used as integration subdomains. Some finite elements, in blue, are added in the representation to show the difference between the integration subdomains and elements. (For interpretation of the references to colour in this figure legend, the reader is referred to the Web version of this article.)

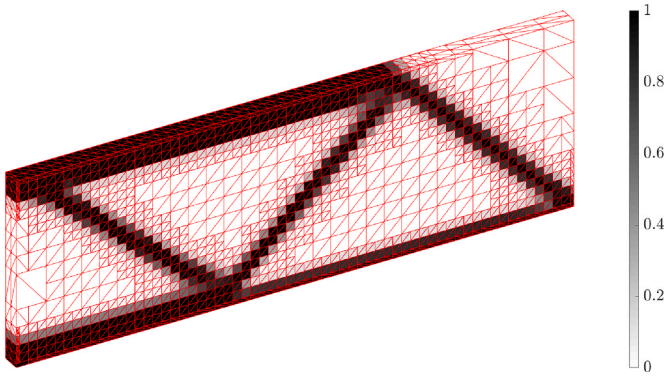

Fig. 13. MBB Problem. Optimal material distribution layout from the topology optimization algorithm, obtained with an *h*-adapted mesh of non-conforming hexahedra of sizes $h_{\mathbb{TO}} = \{0.4782, 0.9563, 1.9126\}$, represented on the conforming tetrahedra used as integration subdomains.[2].

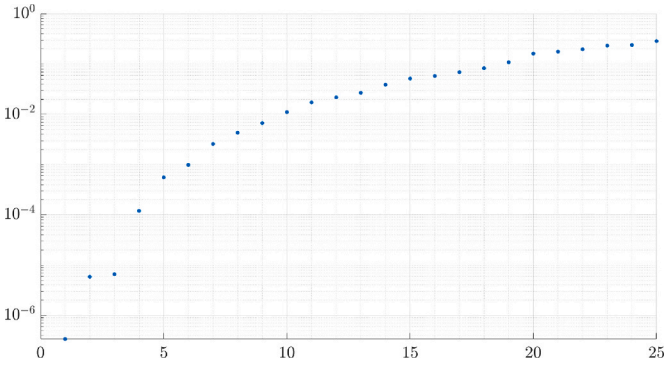

Fig. 14. First 25 eigenvalues of the **M** (see (6)), belonging to the LLE procedure.

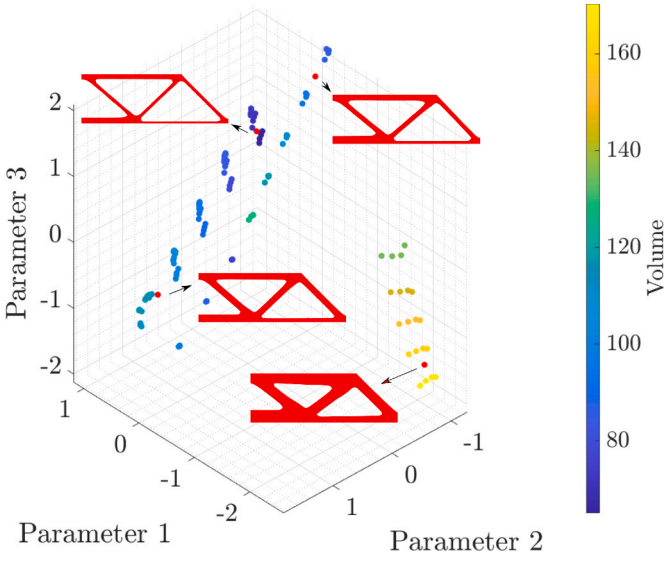

Fig. 15. MBB problem. Embedded space for the reference problem considering $K = 30$ neighbours and $d = 3$ parameters. The colours show the volume of each individual. Additionally, some individuals are visualized with its CAD geometry representation. (For interpretation of the references to colour in this figure legend, the reader is referred to the Web version of this article.)

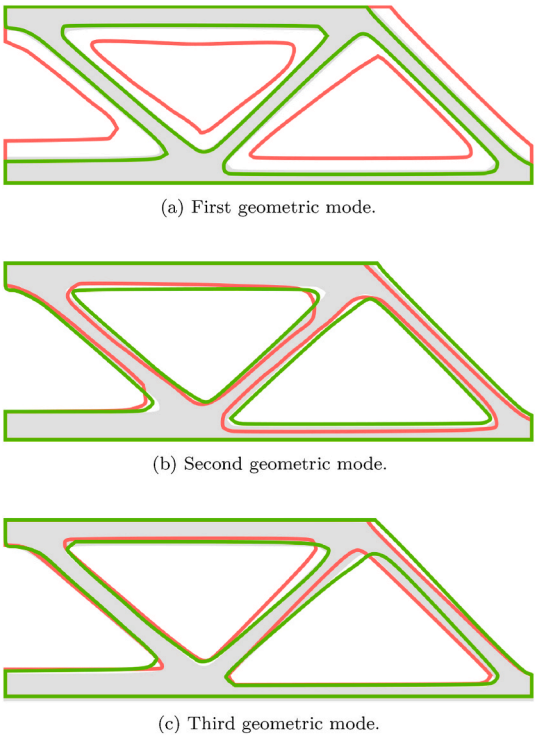

(a) First geometric mode.

(b) Second geometric mode.

(c) Third geometric mode.

Fig. 16. Influence of each geometry mode in the new generated geometries. The reference geometry, obtained from the mean values of the range of each parameter, is represented in grey. We show the variation of each geometric mode by representing their lower and upper values, in red and green colour, respectively. (For interpretation of the references to colour in this figure legend, the reader is referred to the Web version of this article.)

are able to use a wide range of shape optimization algorithms. In this work, we use, for the numerical examples, the Bayesian optimization algorithm. Additionally, other approaches are available such as Genetic Algorithms or Gradient-based algorithms. Fig. 9a shows the optimal geometry of the reference problem, and Fig. 9b represents the recovered von Mises stress field. These results are obtained using a mesh of element size $h_{\mathbb{TO}} = h_{\mathbb{SO}} = 0.9563$, for both optimization algorithms.

The results shown in Fig. 9 satisfy that the maximum stress value is equal to the stress limit (S_y). However, the optimal geometry is far from the analytical optimum. As the optimization process is guided by the FE numerical results, we need to improve their quality to improve the accuracy of the optimal solution. One strategy to improve the solution is to reduce the element size of the FE analysis mesh. If we consider that the main objective TO algorithm is to obtain the preform of the solution, i.e. a definition of its topology, the TO algorithm does not require the use of fine discretizations, therefore, we focus the solution improvement on the shape optimization step, the step that will finally define the geometry. The optimal solution shown in Fig. 10 was computed with an element size of $h_{\mathbb{TO}} = 0.9563$ for the topology optimization algorithm and an element size of $h_{\mathbb{SO}} = 0.2391$ for the shape optimization.

As in the previous analysis, the maximum von Mises stress value is equal to the prescribed yield limit, but in this case the optimal radius we get is far closer to the optimal analytic solution. In order to understand the influence of the mesh in the accuracy and performance, in Table 1 we compare the time consumed in each optimization along with the relative error with the optimal analytic solution. Table 1 includes the analyses whose FE meshes correspond to $h_{\mathbb{TO}} = h_{\mathbb{SO}} = 0.9563$, $h_{\mathbb{TO}} = 0.9563$ with $h_{\mathbb{SO}} = 0.4781$, $h_{\mathbb{TO}} = 0.9563$ with $h_{\mathbb{SO}} = 0.2391$, $h_{\mathbb{TO}} = h_{\mathbb{SO}} = 0.4781$, $h_{\mathbb{TO}} = 0.4781$ with $h_{\mathbb{SO}} = 0.2391$ and $h_{\mathbb{TO}} = h_{\mathbb{SO}} =$

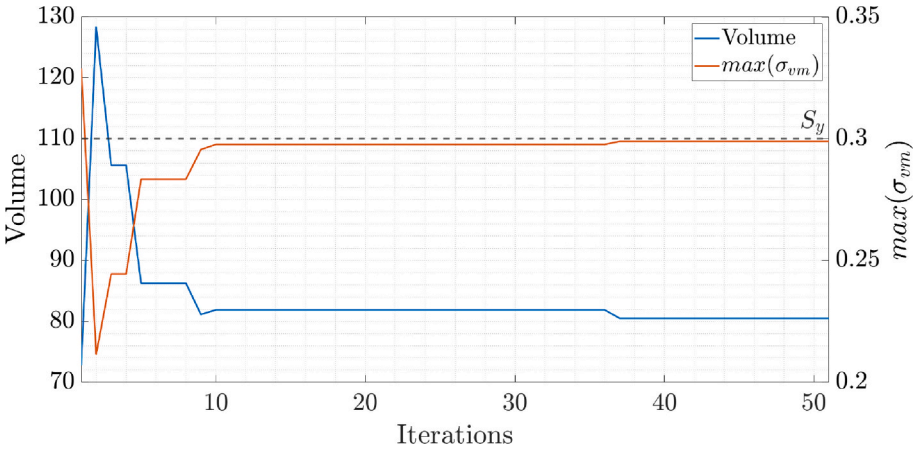

Fig. 17. MBB problem. Convergence graph of the Bayesian optimization algorithm.

0.2391. Additionally, in Fig. 2, we gather the optimal geometry obtained with each of the analysis and compare it with the optimal analytic solution (see Table 2).

Table 1 and Fig. 2 show that, for this problem:

- Obviously, the largest influence on the time taken for the Model Generation ($\mathbb{MG}$) comes from the size of the elements used by the TO process.
- The last column of Table 1 shows that, although smaller values of $h_{\mathbb{TO}}$ lead to more accurate results, the main influence on the accuracy comes from the $h_{\mathbb{SO}}$, the size of the elements used for the SO process.

5. Numerical examples

After having shown the results provided by the proposed hybrid optimization algorithm for the academic reference problem, in this Section, we will use two additional examples. Specifically, we will use the well-known MBB problem and a hook problem.

5.1. MBB problem

Let us consider the well-known "MBB-Beam" problem to illustrate the proposed procedure. To reduce computational cost only half of the beam has been modelled, considering the symmetry of the problem, as shown in Fig. 11. Additionally, in order to consider Plane Strain behaviour, the surface shown in front and its opposite are constrained in its normal direction. Also in Fig. 11, we represent the geometrical dimensions of the design space and the boundary conditions. In particular, the beam is bi-supported and subjected to a parabolic pressure P, whose maximum value equals $P_{\max} = 1$. As the elastic properties of the material, we consider a Young's Modulus $E = 1000$, a Poisson's ratio $\nu = 0.3$ and a yield limit $S_y = 0.3$.

The first step of the procedure is to run the topology optimization algorithm that will provide the optimal material distribution layout to be used as preform. The analysis was been carried out considering a initial mesh with elements of uniform size $h_{\mathbb{TO}} = 0.9563$ and a filter radius set to $r_f = 1.5h_{\mathbb{TO}} = 1.4345$. In Fig. 12 we show the optimal material distribution provided by the topology optimization algorithms.

From Fig. 12, we consider that the preform provided by the topology optimization algorithm lacks of enough boundary definition as the diffuse region (elements with intermediate densities) represents a high percentage of the total design domain. As shown in Ref. [32], h-adaptive mesh refinement strategies allow to enhance the boundary resolution and to improve the solution's quality. In *cgFEM* we can consider two refinement strategies, a) a density-based refinement, where elements with intermediate values of relative density are refined to sharpen the boundary definition, and b) a quality-based refinement where the mesh refinement is guided by the estimated error in energy norm. In this particular case, we harness the density-based refinement strategy to improve the boundary definition, since the shape optimization algorithm will be in charge of the quality of the solution, as explained in Section 4.3. We need to define an acceptable error level to ensure the proper convergence of the Algorithm 2. In this example we prescribed a maximum estimated relative error on energy norm $\eta_{\max} = 12.5\%$ [32]. With these considerations, we analyzed the MBB problem with an initial mesh with elements of uniform size $h^1_{\mathbb{TO}} = 0.9563$ and a filter radius set to $r^1_f = 1.5h^1_{\mathbb{TO}} = 1.4345$ and a second h-adapted mesh with elements of size $h^1_{\mathbb{TO}}$ and $h^2_{\mathbb{TO}} = 0.4782$ and an adaptive filter radius with lengths of r^1_f and $r^2_f = 1.5h^2_{\mathbb{TO}} = 0.7173$. The resulting material distribution layout is shown in Fig. 13, that shows a sharper boundary definition, and a final relative error in energy norm of $\eta = 12.0839\%$.

As in the Reference benchmark problem, once the preform is defined by the topology optimization algorithm, we train the reduced model with the material distributions obtained during the topology optimization process. To accomplish this, we use the LLE algorithm with a vicinity $K = 30$ over a total of 140 points (snapshots). Later, we define the number of dimensions of the embedded space taking into account the eigenvalues obtained from the LLE procedure. In this case, we considered $d = 3$ because the first three eigenvalues were isolated from the rest, as shown in Fig. 14. Fig. 15 represents the resulting embedded space along with several geometries to illustrate the results.

In Fig. 16, we show the reference geometry (obtained with the mean values of the range achieved for each of the three parameters considered) in grey, and the variation of each geometric mode between its lower and upper limit, in red and green colours, respectively. As shown, the variation of the parameters do not only imply the erosion of the structure but also variation of the bars' angles and non-uniform bar sections variations.

With the low-dimensional space properly defined, the shape optimization algorithm will use it as a design space. We used a Bayesian algorithm to update the design variables until the convergence criterion was satisfied. The analysis was carried out with an initial uniform mesh with element size equal $h^1_{\mathbb{SO}} = 0.4782$. In order to get a solution with a high quality, we use an h-adaptive refinement strategy based on the error, specifically we enforce the maximum estimated relative error to $\eta_{\max} = 6\%$. Hence, we allow following h-adapted meshes with elements

[2] Note that some elements have been coarsened as they do not influence the overall error.

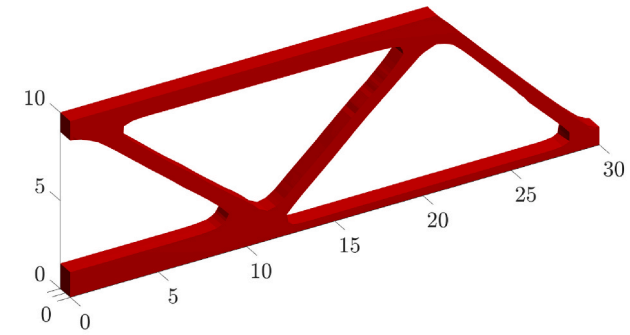

(a) Representation of the optimal geometry.

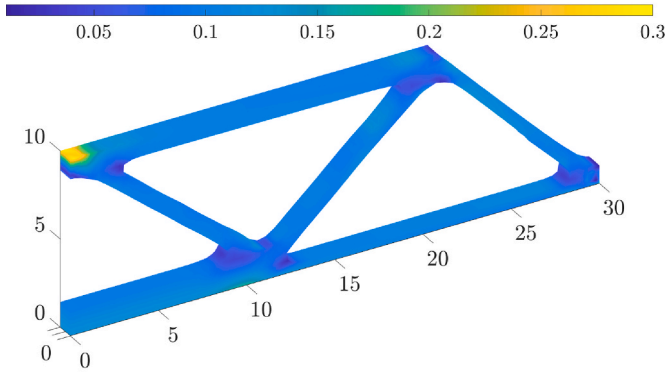

(b) Solution of the von Mises stress field.

Fig. 18. MBB Problem. Hybrid optimization optimal geometry (a) and the corresponding recovered von Mises stress field (b).

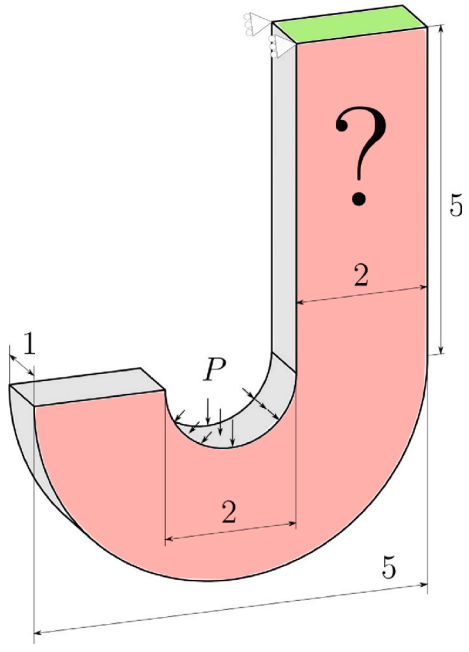

Fig. 19. Hook Problem. Problem representation with geometrical dimensions. Essential boundary conditions imposed over the green surface and symmetry on the red surface, also a parabolic pressure with maximum value $P = 1$ is imposed in the inner cylindrical surface. (For interpretation of the references to colour in this figure legend, the reader is referred to the Web version of this article.)

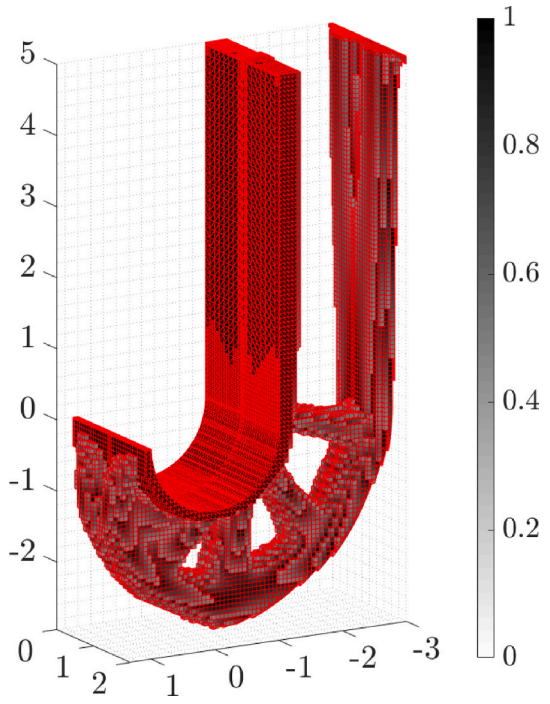

Fig. 20. Hook Problem. Optimal material distribution layout obtained from the topology optimization algorithm, represented on the conforming tetrahedra used as integration subdomains. Notice that integration subdomains whose elemental density is $\rho_e < 0.5$ are discarded from the representation.

of size $h^1_{\mathbb{SO}}$ and $h^2_{\mathbb{SO}} = 0.2391$. The evolution of the optimization process through the Bayesian algorithm is represented in Fig. 17. The optimal CAD geometry is shown in Fig. 18a, while, in Fig. 18b, we display the corresponding recovered von Mises stress field, calculated with a final relative error in energy norm of $\eta = 5.4659\%$.

As shown in Fig. 18a, we obtained a CAD representation of the MBB problem, which is directly suitable for manufacturing. Furthermore, in Fig. 18b, we represented the von Mises stress field whose maximum value is equal to the yield limit $S_y = 0.3$.

5.2. *Hook problem*

The second example corresponds to a hook as displayed in Fig. 19. The essential boundary conditions are imposed over the green surface, while we consider symmetry on the red surface. Rigid body motion is avoided using appropriate constraints on these surfaces. A parabolic

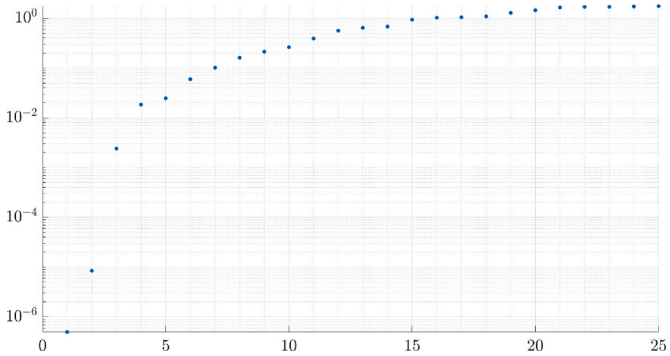

Fig. 21. Hook Problem. Eigenvalues of the LLE method that define the quantity of independent geometrical modes.

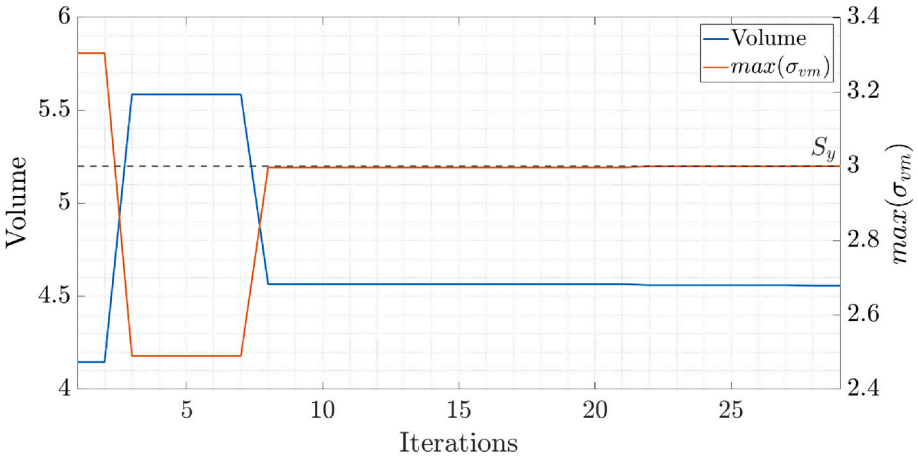

Fig. 22. Hook problem. Convergence graph of the Bayesian optimization algorithm.

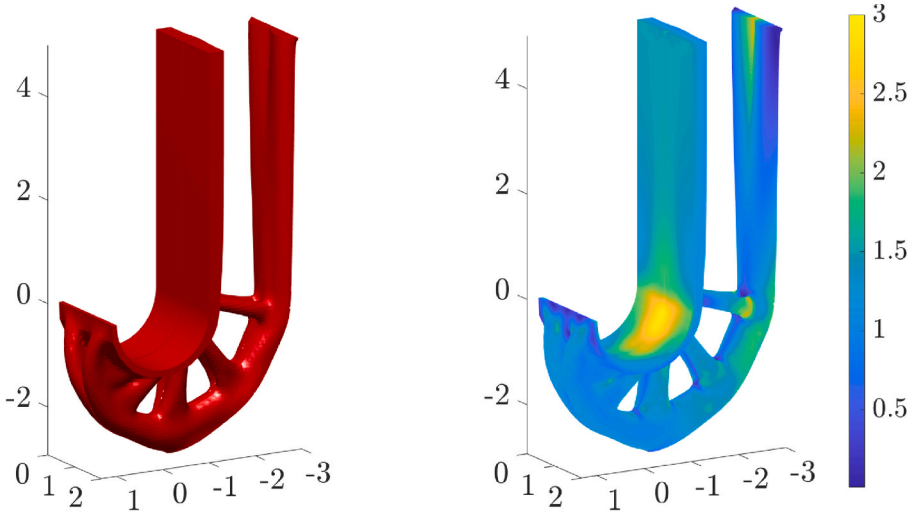

(a) Representation of the optimal geometry. (b) Solution of the von Mises stress.

Fig. 23. Hook Problem. Representation of the result obtained: optimal geometry (a) and von Mises stress field (b).

pressure with a maximum value $P = 1$ is imposed in the inner cylindrical surface. The material properties considered in this problem are: Young's Modulus $E = 1000$, Poisson's ratio $\nu = 0.3$ and yield limit $S_y = 3$.

As in previous examples, the process starts with the topology optimization algorithm. As in the MBB problem, we consider density and error-based h-adaptive refinement with a prescribed maximum estimated relative error in energy norm equal to $\eta_{\max} = 7.5\%$. Specifically, we consider an initial mesh with uniform size $h^1_{\mathbb{TO}} = 0.1275$ and a second h-adapted mesh with elements size $h^1_{\mathbb{TO}}$ and $h^2_{\mathbb{TO}} = 0.0637$. In Fig. 20 we represent the optimal material distribution provided by the TO algorithm, obtained with a final relative error $\eta = 5.9703\%$.

Once the preform is defined by the topology optimization algorithm, we obtain the embedded manifold. As previously, we use the LLE algorithm, in this particular case, we consider a vicinity of $K = 12$ neighbours over a total of 60 snapshots. Studying the eigenvalues obtained, represented in Fig. 21, we consider a dimensionality $d = 2$, as the first two eigenvalues are isolated from the rest.

With the reduced embedded space generated from the LLE algorithm, we run the shape optimization algorithm. The analysis is calculated with an initial uniform mesh of size $h^1_{\mathbb{SO}} = 0.0637$ and an h-adapted refinement strategy that allows following meshes with element size $h^1_{\mathbb{SO}}$ and $h^2_{\mathbb{SO}} = 0.03185$, and a prescribed maximum relative error in energy norm $\eta_{\max} = 3\%$. For this example, we also use a Bayesian optimization algorithm. The iterative process is represented in Fig. 22 and the results we obtained are shown in Fig. 23, which are calculated with a final relative error of $\eta = 2.7010\%$.

6. Conclusion

In order to conclude the current work, we would like to synthesize some final remarks:

- Shape optimization algorithms based on parametrized geometrical representations provide manufacturable solutions but are unable to explore topologies other that the topology described by the prescribed parametrized geometrical model.
- The topology optimization algorithms based on the extensively used SIMP method for structural optimization provide a material distribution that characterizes the topology of the solution. However, this material distribution is not directly suitable for manufacturing.

- In this paper we have proposed a hybrid structural optimization methodology that allies TO and SO algorithms to obtain a synergetic combination of both techniques. This hybrid methodology would represent a more general and powerful structural optimization framework.
- The key aspect of this methodology is the use of a machine learning algorithm to automatically bridge TO and SO algorithm.
- The use of a manifold learning technique, such as the LLE, allowed us to extract the geometrical modes defined by the material distribution information provided by the TO algorithm. In order to correctly use these techniques, the data must be adequately processed. We trans-form the quasi-boolean material distribution into a richer level-set with the information of the distance of each node to the boundary.
- The existence of a latent embedded space among the material distribution data, allows to extract the geometrical modes that define the solution of the TO algorithm. These modes can then define a parametric geometrical model that will be used to create brand new geometries topologically equivalent to each other.
- The geometry parametrization tool developed in this work may be guided by a user or by an algorithm. In case the tool is managed by a parametrized shape optimization algorithm, this algorithm will consider the embedded space as its design space.

Availability of data

Data available on request from the authors. The data that supports the findings of this study are available from the corresponding authors upon reasonable request.

Author statement

D. Muñoz: Methodology, Software, Validation, Investigation, Data Curation, Writing - Original Draft. **E. Nadal**: Conceptualization, Methodology, Investigation, Writing - Review & Editing. **J. Albelda**: Conceptualization, Methodology. **F. Chinesta**: Conceptualization, Writing - Review & Editing. **J.J. Ródenas**: Conceptualization, Methodology, Writing - Review & Editing, Supervision, Funding acquisition.

Declaration of competing interest

The authors declare that they have no known competing financial interests or personal relationships that could have appeared to influence the work reported in this paper.

Acknowledgements

The authors gratefully acknowledge the financial support of Ministerio de Educación y Formación Profesional (FPU16/07121), Generalitat Valenciana (Prometeo/2021/046), Ministerio de Economía, Industria y Competitividad (DPI2017-89816-R) and FEDER.

A. Appendices

A.1. Appendix: Topology Optimization

Topology optimization tries to find the optimal material distribution layout over a given physical design domain. As it belongs to the structural optimization field, it handles the minimization of an objective function subjected to the satisfaction of a set of constraints. The topology optimization problem is defined over a design domain, thus it is characterized by a large set of design variables, as any element of the discretization may be material or void. Thanks to the consideration of the fictitious material as a composite behaviour [36] where the elastic properties are defined through a characteristic function, topology optimization has become widely used. The Solid Isotropic Material Penalization (SIMP) method regularizes the material properties as a penalization of the density interpolation function. In addition to the SIMP method, there exist other techniques in the bibliography: strictly based in the 0–1 values of relative density [37–40], level-set based on the nodal values of an implicit function [41–45] and based on the phase-field [46], for instance.

In structural topology optimization we compute the optimal material distribution ρ in a given design domain Ω, which is defined as a continuous variable bounded between 0 (void) and 1 (material). When the structural topology optimization problem is solved using the SIMP method, introduced in Refs. [1–3], usually, the optimization problem consists in minimizing the compliance $c(\rho)$ subject to certain constraints concerning the amount of material. In order to enforce the material/void segregation as much as possible, the method uses a penalization parameter p to penalize intermediate density values. Thus, the SIMP method considers the following optimization problem:

$$
(\mathbb{TO}(v_f)) = \begin{cases}
\min\limits_{\rho,u}: & c(\rho;\mathbf{u}) = \dfrac{1}{2}\displaystyle\int_\Omega \boldsymbol{\varepsilon}(\mathbf{u})\mathbf{D}(\rho)\boldsymbol{\varepsilon}(\mathbf{u})d\Omega & \text{(10a)}\\
& \text{with} \quad \mathbf{D}(\rho) = \rho^p\mathbf{D}_0 & \text{(10b)}\\
\text{subject to:} & V(\rho) = \displaystyle\int_\Omega \rho d\Omega = \overline{V}_e\sum\rho_e = v_f V_0 & \text{(10c)}\\
& a(\mathbf{u},\boldsymbol{\nu};\rho) = l(\boldsymbol{\nu}) \text{ where,} & \text{(10d)}\\
& a(\mathbf{u},\boldsymbol{\nu};\rho) = \displaystyle\int_\Omega \boldsymbol{\varepsilon}(\mathbf{u})\mathbf{D}(\rho)\boldsymbol{\varepsilon}(\boldsymbol{\nu})d\Omega & \text{(10e)}\\
& l(\boldsymbol{\nu}) = \displaystyle\int_\Omega \mathbf{b}^T\boldsymbol{\nu}d\Omega + \int_{\Gamma_N}\mathbf{t}^T\boldsymbol{\nu}d\Gamma_N & \text{(10f)}\\
& 0 \leq \rho_{min} \leq \rho \leq 1, & \text{(10g)}
\end{cases}
$$

considering Voigt's notation $\boldsymbol{\varepsilon}$ is the strain field, $\mathbf{u}$ is the displacement field and $\boldsymbol{\nu}$ is the test function. $\mathbf{D}$ is the matrix of the Hooke's law that relates strains $\boldsymbol{\varepsilon}$ and stresses $\boldsymbol{\sigma}$. As shown in the equation, in the SIMP $\mathbf{D}$ is defined as a function of $\mathbf{D}_0$ (the matrix of the Hooke's law for the fully dense material), the density field ρ and the penalization parameter p. Additionally, v_f is a prescribed volume fraction and V_0 is the total volume of the design domain. Finally, an additional side-constraint is added on ρ.

In Algorithm 1, we show the structure of the SIMP method with the compliance c as a objective function and the volume fraction as constraint. Additionally, we remark the need of a filtering technique to avoid numerical instabilities, in this case sensitivities filtering. Finally, the use of an

updating scheme f to obtain a new set of design variables ρ_{i+1}, such as the Optimality Criteria (OC) [47], is also required.

Algorithm 1
$\mathbb{TO}(v_f)$.Compliance minimization algorithm.

Define v_f
Initialize counter: $i = 0$
Initialize relative density at each element e: $\rho_{e_i} = v_f$
$Repeat = 1$
while $Repeat = 1$ **do**
  Run FE analysis
  Obtain compliance, c_i, and sensitivities , $\partial c_i/\partial \rho_{e_i}$
  Filter sensitivities
  Update relative density field: $\rho_{e_{i+1}} = f(\rho_{e_i}, \partial c_i/\partial \rho_{e_i})$
  if $\|\rho_{e_{i+1}} - \rho_{e_i}\|_\infty \leq tolerance$ **then**
    $Repeat = 0$
  end
  $i = i + 1$
end

For the sake of simplicity, we implemented a very basic, not necessarily efficient algorithm (Algorithm 2) that performs a heuristic stress scaling procedure [32], whose behaviour has been checked for the examples presented in this paper. The proposed algorithm allows us to explore different volume fraction following a simple stress scaling procedure where the volume fraction is adapted to target a predefined maximum stress value. In particular, the objective of the implemented algorithm is to find the value of volume fraction that would produce a solution whose maximum von Mises stress targets the value of a critical stress, $max(\sigma^*_{eq}) \equiv S_{crit}$. To accomplish this objective, we define two nested loops, the outer loop will drive the selection of the value of the volume fraction and evaluate if the prescribed level of stress is achieved. Meanwhile, the inner loop will follow the strategy proposed in the original SIMP method, that minimizes the compliance of the component subjected to a volume fraction constraint, whose value has been defined in the outer loop. As our procedure is based on the original SIMP method, we will only consider minimum compliance solutions. The algorithm described above, may be formulated as follows, where we indicate that the problem is subjected to the calculation of the algorithm that describes the SIMP method (Algorithm 1),

$$(\mathbb{TO}(v_f(S_y))) = \begin{cases} \text{find:} & v_f & \text{(11a)} \\ \text{subjected to:} & max(\sigma^*_{eq}) \equiv S_{crit} & \text{(11b)} \\ & \mathbb{TO}(v_f) & \text{(11c)} \end{cases}$$

where S_{crit} is the limit value of σ^*_{eq}. In this work we considered S_{crit} as the yield limit S_y and σ^*_{eq} represents an equivalent uniaxial stress value. In this work, we used as σ^*_{eq} the recovered von Mises stress field σ^*_{vm} evaluated from σ^*, the so called recovered stress field, more accurate than the stress field $\boldsymbol{\sigma}^h$ provided by the FEM. There are different procedures to obtain $\boldsymbol{\sigma}^*$. Because of their accuracy, the most commonly used techniques are the Superconvergent Patch Recovery (SPR) technique (proposed by Zienkiewicz and Zhu [48]) and enhanced versions of this technique, like the SPR-C technique [49].

The use of the density field ρ in topology optimization implies, a particular definition of the stress field to keep consistency with the expression of the strain energy (compliance) in (10a). We can rewrite equation (10a) as:

$$\boldsymbol{\sigma}^{h_\rho}_e = \mathbf{D}(\rho_e)\boldsymbol{\varepsilon}^h_e = \rho^p_e \mathbf{D}_0 \boldsymbol{\varepsilon}^h_e = \rho^p_e \boldsymbol{\sigma}^{h_0}_e \tag{12}$$

where $\boldsymbol{\sigma}^{h_0}_e = \mathbf{D}_0\boldsymbol{\varepsilon}^h_e$ would represent the original FE stress field at the element, before considering the density correction. The penalization parameter p in (12) is consistent with equation (10b) [33,50]. Taking into account equation (12), for the evaluation of the recovered stress field we propose to smooth the original stress field at elements, $\boldsymbol{\sigma}^{h_0}$, and then to modify the resulting recovered stress field using the density correction.

The steps to address the problem in (11) are presented in Algorithm 2. As previously mentioned, the structure of the problem is a nested optimization loop. The outer loop searches for the volume fraction whose corresponding maximum von Mises stress equals the yield limit, while the inner loop minimizes the compliance of the component subjected to the volume fraction defined in the outer loop. For the sake of simplicity, the updating scheme g in Algorithm 2 consists of a quadratic curve fitting procedure. This method uses the information of the last 3 iterations, specifically the values of volume fractions $\overline{v_f}$ and their corresponding stress $\overline{max(\sigma^*_{vm})}$, to fit a surrogate model and infer the next value of v^{i+1}_f that would produce a $max(\sigma^*_{vm}) \equiv S_y$. A schematic representation of this strategy is show in Fig. 24.

Algorithm 2
$\mathbb{TO}(v_f(S_y))$. Stress scaling algorithm for evaluation of volume fraction for which $max(\sigma^*_{vm}) \equiv S_y$, with inner topology optimization loop based on the SIMP method.

Set S_y
Initialize counter: $i = 0$
Initialize volume fraction v_f^i
$Repeat = 1$
while $Repeat = 1$ **do**
  $i = i + 1$
  Run *Algorithm* 1 $\mathbb{TO}(v_f^i)$
  Obtain the stresses of the optimal layout distribution
  Evalute the maximum von Mises stress: $max(\sigma_{vm}^{*i})$
  if $max(\sigma_{vm}^{*i}) \equiv S_y$ **then**
    $Repeat = 0$
  end
  Update the volume fraction: $v_f^{i+1} = g(\overline{v_f}, \overline{max(\sigma_{vm}^*)}, S_y)$
end

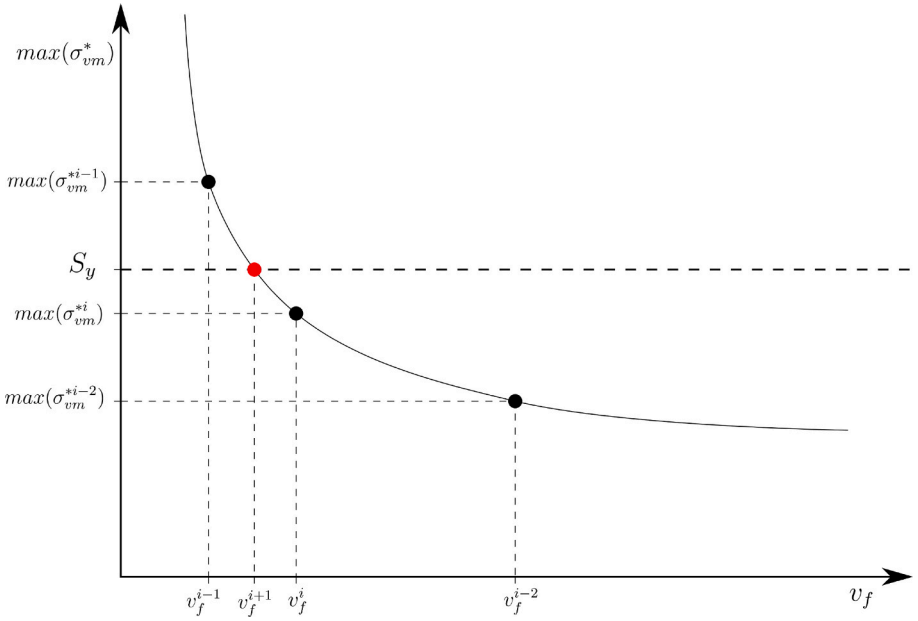

Fig. 24. Schematic representation of the curve fitting procedure (*g* in Algorithm 2). Considering the volume fraction exploration algorithm, we use the value of the last three iterations and its corresponding maximum von Mises stress, and adjust a curve. The volume fraction value for which this curve will reach the value of the yield limit (S_y) corresponds to the next value of volume fraction.

A.2. Appendix: Shape Optimization

In this work we consider the parametrized shape optimization where the boundary is defined *a priori* by means of a set of parameters, also known as design variables $\boldsymbol{a}$, as shown in Fig. 25.

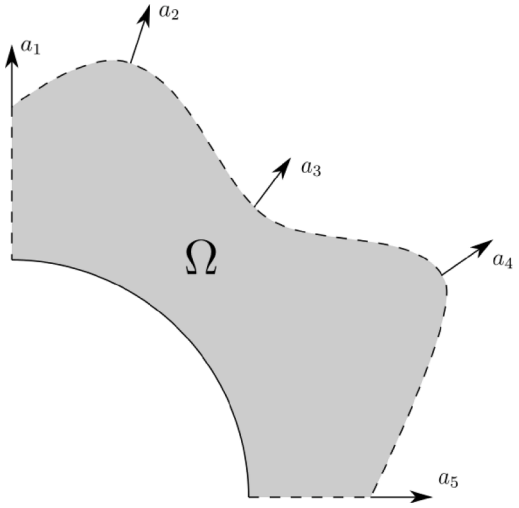

Fig. 25. Parametrized boundary of the design domain.

The shape optimization formulation applied to the structural behaviour commonly uses the volume or mass as the objective function and a given measure of the stresses as a constraint, for instance to keep the maximum von Mises stress $max(\sigma^*_{vm})$ below the yield stress limit S_y, as follows:

$$(\mathbb{SO}_\sigma(S_y)) = \begin{cases} \min\limits_{a}: & \text{Volume}(a) & \text{(13a)} \\ \text{subjected to:} & max(\sigma^*_{vm}(a)) \leq S_y & \text{(13b)} \end{cases}$$

A.3. Appendix: Dimensionality Reduction

The data in most fields of science and engineering has high dimensionality. In order to manage high quantity of data and to handle it adequately, its dimension must be reduced. Dimensionality Reduction (DR) techniques are a set of algorithms that transform the high-dimensional data into a reduced space. This manifold preserves the original structure of the high-dimensional space by extracting the main principal characteristics. The dimensionality reduction eases the classification, visualization or even understanding of the high-dimensional data. Additionally, in this work the reduced dimensions are used to generate new high-dimensional data, not existing in the original dataset. Linear techniques, such as Principal Component Analysis (PCA) were initially used to perform the dimensionality reduction. But in last decades, non-linear techniques have been developed to obtain the manifold space. The advantage of this techniques is that they are able to transform complex non-linear data. We propose the use of the Locally Linear Embedding (LLE). Fig. 26 shows how it maintains the structure of a given dataset.

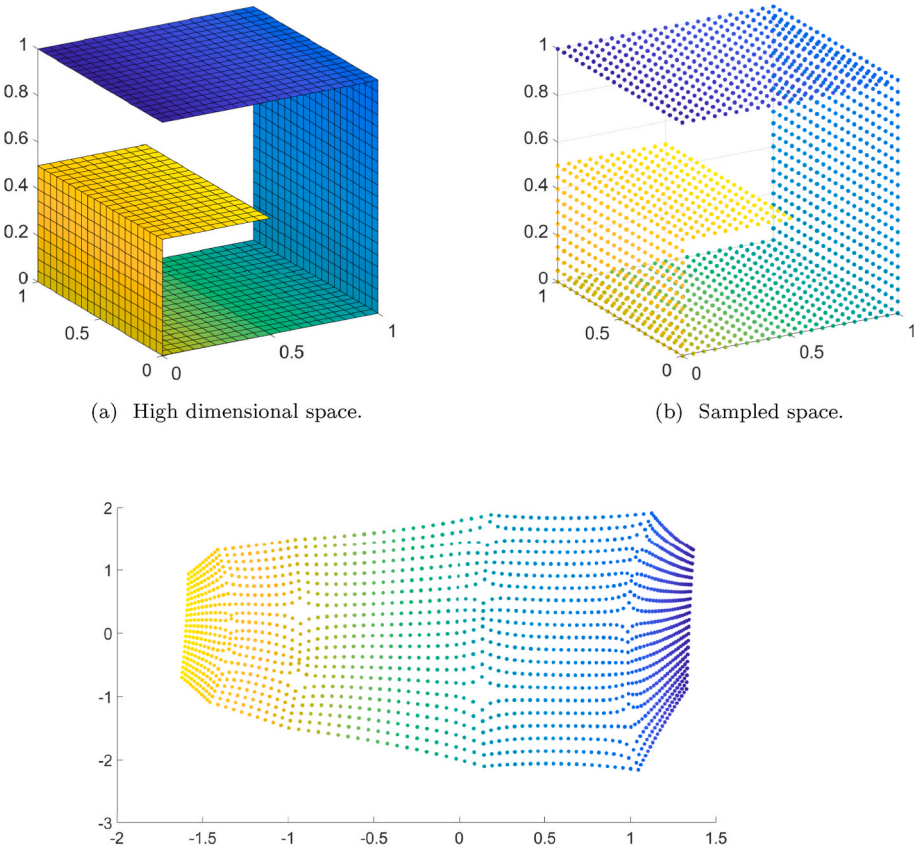

(a) High dimensional space.

(b) Sampled space.

(c) Embedded space.

Fig. 26. Example of the LLE algorithm, (a) represents the original high dimensional data, (b) shows a sampled space from the high dimensional space and (c) illustrates the embedded manifold provided by the LLE algorithm over the sampled high dimensional space.

A.4. Appendix: Cartesian Grid Finite Element Method (cgFEM)

The accuracy of the FE analysis is a relevant factor in optimization processes but, as these are iterative algorithms, the computational efficiency of the FE analysis is critical. The use of meshes where all the elements have the same shape helps to improve the overall performance of the FE analysis. In these cases, the stiffness matrix evaluated for one element can be used for any other element having the same material properties simply considering a stiffness scaling factor evaluated as a function of the ratio of the element sizes. In fact, in most numerical examples shown in the literature of topology optimization, the domain used for the optimization is a rectangle (2D) or a cuboid (3D), as these shapes can be easily meshed with Cartesian elements. However, practical applications cannot be restricted to this kind of domains. If standard boundary-conforming FE meshes were used, it would not be possible to ensure that all the elements have the same shape. The use of Fictitious Domain Methods (FDM), where the FE mesh is not necessarily conforming to the geometry, like the Finite Cell Method [26–28] or the Cartesian grid finite element method (*cgFEM*) [24,25], both of them based on the use of Cartesian grids, is an alternative to solve this issue.

In particular, in *cgFEM* we embed the physical domain, Ω_{Phys}, in a cuboid defining the fictitious domain, Ω_{Fic}. The fictitious domain is meshed with elements of different levels. Considering the *Level-0* mesh as a single element embedding the cuboid, we split the mesh into 8 new Cartesian elements that structure the *Level-1* mesh. We repeat the same process recursively to create meshes with higher refinement levels, so they have a hierarchical structure. Then, the mesh for the FE analysis is created with elements of different levels of refinement. In order to impose C^0 continuity between contiguous elements from different level, we use multi-point constraints.

Fig. 27 a represents an example of physical domain, Ω_{Phys}, with a sufficiently smooth boundary Γ, embedded into the embedding domain Ω_{Fic}. The boundary Γ of Ω_{Phys} can be divided into two non-overlapping parts, Γ_D and Γ_N, where the Dirichlet and Neumann conditions are respectively imposed. Fig. 27b, shows the embedding domain Ω_{Fic}, discretized with Cartesian elements. The following expression relates the different domains:

$$\Omega_{Phys} \subseteq \Omega_{Fic} = \bigcup_{e=1}^{n_e} \Omega^e \tag{14}$$

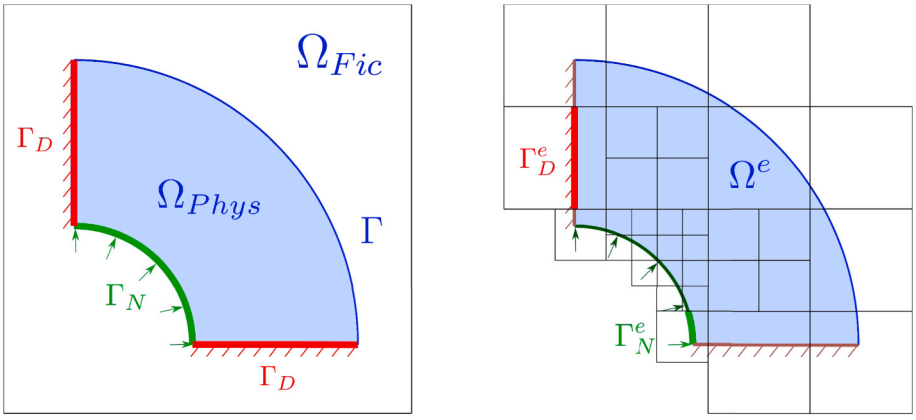

(a) Physical and embedding domains. Boundary conditions.

(b) Discretization of the fictitious domain.

Fig. 27. Cartesian grid finite element method (*cgFEM*). Representation of the physical domain and the discretization of the fictitious domain.

Fig. 28 shows a 3D example analyzed with *cgFEM* that is used here to summarize the main characteristics of this methodology:

- *cgFEM* is an efficient FE analysis technique as it considers a Cartesian discretization of the embedding domain (see Fig. 28a).
- The analysis mesh used by *cgFEM* to model the physical domain Ω_{Phys} can consider elements of different refinement levels. These elements include elements fully placed into Ω_{Phys} and elements cut by its boundary Γ. Elements fully outside of Ω_{Phys} are not considered in the analysis mesh (see Fig. 28b).
- *cgFEM* uses a specifically designed integration mesh (Fig. 28c), based on the NEFEM integration approach [51] that allows to consider the exact boundary representation given by, for instance, NURBS or T-Splines [52].

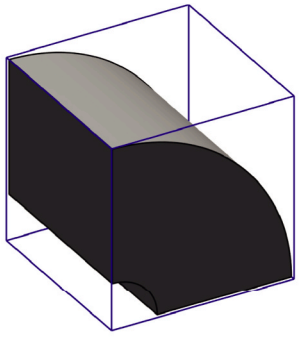

(a) Physical domain Ω_{Phys} (Cylinder) embedded in the fictitious domain Ω_{Fic} (cube).

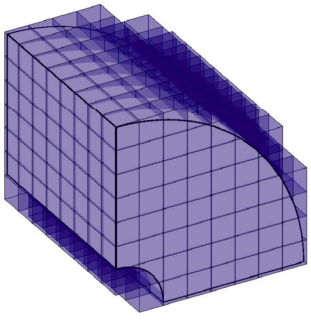

(b) Discretization of the fictitious domain: analysis mesh.

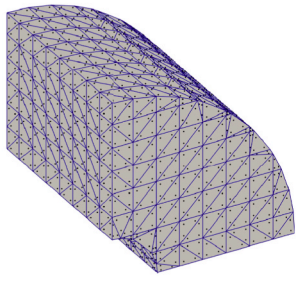

(c) Integration Mesh.

Fig. 28. *cgFEM*. Different domains involved in a finite element analysis.

A stabilized Lagrange multipliers formulation is used to impose boundary conditions in elements cut by the Dirichlet boundary. As a result, equation (10d) is replaced by the following equation,

$$a(\mathbf{u},\boldsymbol{\nu})+\frac{k}{h}\int_{\Gamma_D}\mathbf{u}\cdot\boldsymbol{\nu}d\Gamma=l(\boldsymbol{\nu})+\frac{k}{h}\int_{\Gamma_D}\mathbf{g}\cdot\boldsymbol{\nu}d\Gamma+\int_{\Gamma_D}\mathbf{T}(\bar{\mathbf{u}})\cdot\boldsymbol{\nu}d\Gamma \tag{15}$$

A detailed description of the derivation of this equation and the description of its behaviour, out of the scope of this paper, can be found in Ref. [53]. The most relevant feature of the proposed stabilized Lagrange multipliers formulation is that the stabilization term **T** is evaluated as a recovered [48,49] traction field. As this traction field depends on the FE solution, an iterative process, i.e. Richardson iterations, is used to solve (15). The stabilization terms are not affected by ρ and do not play any role in the TO procedure.

References

[1] M.P. Bendsøe, Optimal shape design as a material distribution problem, Struct. Optim. 1 (4) (1989) 193–202.
[2] M. Zhou, G.I. Rozvany, The COC algorithm, Part II: topological, geometrical and generalized shape optimization, Comput. Methods Appl. Mech. Eng. 89 (1–3) (1991) 309–336.
[3] H.P. Mlejnek, Some aspects of the genesis of structures, Struct. Optim. 5 (1–2) (1992) 64–69.
[4] M.Y. Wang, X. Wang, D. Guo, A level set method for structural topology optimization, Comput. Methods Appl. Mech. Eng. 192 (1–2) (2003) 227–246.
[5] M.Y. Wang, X. Wang, Color" level sets: a multi-phase method for structural topology optimization with multiple materials, Comput. Methods Appl. Mech. Eng. 193 (6–8) (2004) 469–496.
[6] L. Shu, M. Yu Wang, Z. Ma, Level set based topology optimization of vibrating structures for coupled acoustic-structural dynamics, Comput. Struct. 132 (2014) 34–42.
[7] L. Dedè, M.J. Borden, T.J. Hughes, Isogeometric analysis for topology optimization with a phase field model, Arch. Comput. Methods Eng. 19 (3) (2012) 427–465.
[8] A.L. Gain, G.H. Paulino, Phase-field based topology optimization with polygonal elements: a finite volume approach for the evolution equation, Struct. Multidiscip. Optim. 46 (3) (2012) 327–342.
[9] S.H. Jeong, G.H. Yoon, A. Takezawa, D.H. Choi, Development of a novel phase-field method for local stress-based shape and topology optimization, Comput. Struct. 132 (2014) 84–98.
[10] M. Papadrakakis, B.H. Topping, Innovative Computational Methods for Structural Mechanics, Saxe-Coburg Publications, 1999.
[11] P.S. Tang, K.H. Chang, Integration of topology and shape optimization for design of structural components, Struct. Multidiscip. Optim. 22 (1) (2001) 65–82.
[12] G.W. Jang, K.J. Kim, Y.Y. Kim, Integrated topology and shape optimization software for compliant MEMS mechanism design, Adv. Eng. Software 39 (1) (2008) 1–14.
[13] A.R. Yildiz, N. Öztürk, N. Kaya, F. Öztürk, Integrated optimal topology design and shape optimization using neural networks, Struct. Multidiscip. Optim. 25 (4) (2003) 251–260.
[14] M. Bremicker, M. Chirehdast, N. Kikuchi, P.Y. Papalambros, Integrated topology and shape optimization in structural design, Mech. Struct. Mach. 19 (4) (1991) 551–587.
[15] G.A. Méndez Algarra, A. Tovar Pérez, Integrating topology and shape optimization: a way to reduce weight in structural ship design, Cien. Tecn. Buques 3 (2009) 83–92.
[16] M.P. Bendsøe, H.C. Rodrigues, Integrated topology and boundary shape optimization of 2-D solids, Comput. Methods Appl. Mech. Eng. 87 (1) (1991) 15–34.
[17] M. Zhou, N. Pagaldipti, H.L. Thomas, Y.K. Shyy, An integrated approach to topology, sizing, and shape optimization, Struct. Multidiscip. Optim. 26 (5) (2004) 308–317.
[18] A.N. Christiansen, J.A. Bærentzen, M. Nobel-Jørgensen, N. Aage, O. Sigmund, Combined shape and topology optimization of 3D structures, Comput. Graph. 46 (2015) 25–35.
[19] T.T. Nguyen, J.A. Bærentzen, O. Sigmund, N. Aage, Efficient hybrid topology and shape optimization combining implicit and explicit design representations, Struct. Multidiscip. Optim. 62 (3) (2020) 1061–1069.
[20] L. Jiang, S. Chen, X. Jiao, Parametric shape and topology optimization: a new level set approach based on cardinal basis functions, Int. J. Numer. Methods Eng. 114 (1) (2018) 66–87.
[21] N. Ferro, S. Micheletti, S. Perotto, An optimization algorithm for automatic structural design, Comput. Methods Appl. Mech. Eng. 372 (2020) 113335.
[22] I.T. Jolliffe, Springer series in statistics, Princ. Comp. Anal. 98 (2002) 487, second ed.
[23] S.T. Roweis, L.K. Saul, Nonlinear dimensionality reduction by locally linear embedding, Science 290 (5500) (2000) 2323–2326.
[24] E. Nadal, J.J. Ródenas, J. Albelda, M. Tur, J.E. Tarancón, F.J. Fuenmayor, Efficient Finite Element Methodology Based on Cartesian Grids: Application to Structural Shape Optimization, vol. 2013, Abstract and Applied Analysis, 2013, pp. 1–19.
[25] E. Nadal, Cartesian grid FEM (cgFEM): high performance h-adaptive FE analysis with efficient error control, Appl. Struct. Shape Optim. (2014) 312.
[26] J. Parvizian, A. Düster, E. Rank, Finite cell method : h- and p-extension for embedded domain problems in solid mechanics, Comput. Mech. 41 (1) (2007) 121–133.
[27] A. Düster, J. Parvizian, Z. Yang, E. Rank, The finite cell method for three-dimensional problems of solid mechanics, Comput. Methods Appl. Mech. Eng. 197 (45–48) (2008) 3768–3782.
[28] J. Parvizian, A. Düster, E. Rank, Topology optimization using the finite cell method, Optim. Eng. 13 (1) (2012) 57–78.
[29] J.E. Shigley, C.R. Mischke, R.G. Budynas, Shingle's Mechanical Engineering Design, PhD thesis, ninth ed., 2002.
[30] D. González, E. Cueto, F. Chinesta, Computational patient Avatars for surgery planning, Ann. Biomed. Eng. 44 (1) (2016) 35–45.
[31] W.E. Lorensen, H.E. Cline, Marching Cubes: a high resolution 3D surface construction algorithm, Comput. Graph. 21 (4) (1987) 163–169.
[32] D. Muñoz, J. Albelda, J.J. Ródenas, E. Nadal, Improvement in 3D topology optimization with h-adaptive refinement using the Cartesian grid Finite Element Method, Int. J. Numer. Methods Eng. (2021).
[33] C. Le, J. Norato, T. Bruns, C. Ha, D. Tortorelli, Stress-based topology optimization for continua, Struct. Multidiscip. Optim. 41 (4) (2010) 605–620.
[34] D. Yang, H. Liu, W. Zhang, S. Li, Stress-constrained topology optimization based on maximum stress measures, Comput. Struct. 198 (2018) 23–39.
[35] S.T. Roweis, L.K. Saul, Nonlinear dimensionality reduction by locally linear embedding, Science 290 (2000) 2323–2326.
[36] M.P. Bendsøe, N. Kikuchi, Generating optimal topologies in structural design using a homogenization method, Comput. Methods Appl. Mech. Eng. 71 (2) (1988) 197–224.
[37] Y.M. Xie, G.P. Steven, A simple evolutionary procedure for structural optimization, Comput. Struct. 49 (5) (1993) 885–896.
[38] P. Tanskanen, The evolutionary structural optimization method: theoretical aspects, Comput. Methods Appl. Mech. Eng. 191 (47–48) (2002) 5485–5498.
[39] D.J. Munk, G.A. Vio, G.P. Steven, Topology and shape optimization methods using evolutionary algorithms: a review, Struct. Multidiscip. Optim. 52 (3) (2015) 613–631.
[40] P.A. Vikhar, Evolutionary algorithms: a critical review and its future prospects, in: 2016 International Conference on Global Trends in Signal Processing, Information Computing and Communication (ICGTSPICC), IEEE, 2016, pp. 261–265.
[41] M.Y. Wang, X. Wang, D. Guo, A level set method for structural topology optimization, Comput. Methods Appl. Mech. Eng. 192 (1–2) (2003) 227–246.
[42] M.Y. Wang, X. Wang, Color" level sets: a multi-phase method for structural topology optimization with multiple materials, Comput. Methods Appl. Mech. Eng. 193 (6–8) (2004) 469–496.
[43] G. Allaire, F. De Gournay, F. Jouve, A.-M. Toader, Structural optimization using topological and shape sensitivity via a level set method, Tech. Rep. (2005).
[44] S. Amstutz, H. Andrä, A new algorithm for topology optimization using a level-set method, J. Comput. Phys. 216 (2) (2006) 573–588.
[45] T. Yamada, K. Izui, S. Nishiwaki, A. Takezawa, A topology optimization method based on the level set method incorporating a fictitious interface energy, Comput. Methods Appl. Mech. Eng. 199 (45–48) (2010) 2876–2891.
[46] L. Dedè, M.J. Borden, T.J. Hughes, Isogeometric analysis for topology optimization with a phase field model, Arch. Comput. Methods Eng. 19 (3) (2012) 427–465.
[47] O. Sigmund, A 99 line topology optimization code written in matlab, Struct. Multidiscip. Optim. 21 (2) (2001) 120–127.
[48] O.C. Zienkiewicz, J.Z. Zhu, The superconvergent patch recovery (SPR) and adaptive finite element refinement, Comput. Methods Appl. Mech. Eng. 101 (1–3) (1992) 207–224.
[49] J.J. Ródenas, M. Tur, F.J. Fuenmayor, A. Vercher, Improvement of the superconvergent patch recovery technique by the use of constraint equations: the SPR-C technique, Int. J. Numer. Methods Eng. 70 (6) (2007) 705–727.
[50] M. Bruggi, On an alternative approach to stress constraints relaxation in topology optimization, Struct. Multidiscip. Optim. 36 (2) (2008) 125–141.
[51] R. Sevilla, S. Fernández-Méndez, A. Huerta, NURBS-enhanced finite element method (NEFEM), Int. J. Numer. Methods Eng. 76 (1) (2008) 56–83.
[52] O. Marco, R. Sevilla, Y. Zhang, J.J. Ródenas, M. Tur, Exact 3D boundary representation in finite element analysis based on Cartesian grids independent of the geometry, Int. J. Numer. Methods Eng. 103 (6) (2015) 445–468.
[53] M. Tur, J. Albelda, O. Marco, J.J. Ródenas, Stabilized method of imposing Dirichlet boundary conditions using a recovered stress field, Comput. Methods Appl. Mech. Eng. 296 (2015) 352–375.